Research
A SCIENCE PARTNER JOURNAL

RESEARCH ARTICLE

Enhanced Sensing Mechanism Based on Shifting an Exceptional Point

Xuan Mao[1†], Guo-Qing Qin[2†], Hao Zhang[3], Bo-Yang Wang[1], Dan Long[1], Gui-Qin Li[1,4], and Gui-Lu Long[1,4,5*]

[1]Department of Physics, State Key Laboratory of Low-Dimensional Quantum Physics, Tsinghua University, Beijing 100084, China. [2]Beijing Institute of Radio Measurement, The Second Academy of China Aerospace Science and Industry Corporation (CASIC), Beijing 100854, China. [3]Purple Mountain Laboratories, Nanjing 211111, China. [4]Frontier Science Center for Quantum Information, Beijing 100084, China. [5]Beijing Academy of Quantum Information Sciences, Beijing 100193, China.

*Address correspondence to: gllong@tsinghua.edu.cn
†These authors contributed equally to this work.

Citation: Mao X, Qin GQ, Zhang H, Wang BY, Long D, Li GQ, Long GL. Enhanced Sensing Mechanism Based on Shifting an Exceptional Point. *Research* 2023;6:Article 0260. https://doi.org/10.34133/research.0260

Submitted 10 August 2023
Accepted 10 October 2023
Published 31 October 2023

Copyright © 2023 Xuan Mao et al. Exclusive licensee Science and Technology Review Publishing House. No claim to original U.S. Government Works. Distributed under a Creative Commons Attribution License 4.0 (CC BY 4.0).

Non-Hermitian systems associated with exceptional points (EPs) are expected to demonstrate a giant response enhancement for various sensors. The widely investigated enhancement mechanism based on diverging from an EP should destroy the EP and further limits its applications for multiple sensing scenarios in a time sequence. To break the above limit, here, we proposed a new enhanced sensing mechanism based on shifting an EP. Different from the mechanism of diverging from an EP, our scheme is an EP nondemolition and the giant enhancement of response is acquired by a slight shift of the EP along the parameter axis induced by perturbation. The new sensing mechanism can promise the most effective response enhancement for all sensors in the case of multiple sensing in a time sequence. To verify our sensing mechanism, we construct a mass sensor and a gyroscope with concrete physical implementations. Our work will deepen the understanding of EP-based sensing and inspire designing various high-sensitivity sensors in different physical systems.

Introduction

Non-Hermitian quantum systems present attractive properties such as exceptional points (EPs) [1–6] at which 2 or more eigenvalues and the corresponding eigenstates coalesce simultaneously [7]. The existence of EPs has been verified in various physical systems such as optomechanical systems [8–10], coupled atom–cavity systems [11], and plasmonic systems [12–14]. The exotic properties of non-Hermitian systems [15–18] open potential possibilities for diverse advanced applications including phonon lasers [9,19–21], chiral mode conversion [8,22–26], and enhanced sensing [3,4,27–32]. The response enhancement at EPs has been widely investigated in microcavities [3,4,29,33], optomechanical systems [31,34,35], and circuits [28,36–38].

Owing to the complex response near an nth-order EP, any small perturbation destroys the degeneracy that results in an nth-root response for the frequency splitting [4]. For sufficiently small perturbation, the splitting is much larger than observed in conventional schemes where the response is proportional to the perturbation strength. The giant enhancement of EPs has been verified both theoretically and experimentally in various detection schemes [3,4,32,39–41] ranging from mass sensor [31] to nanoparticle detector [4,29,32], from magnetometer [34,39] to gyroscope [3,33,35,42–44]. Not only the presence of perturbation will cause the frequency splitting, but also the degeneracy of the linewidths disappears after introducing perturbation. The EP condition is totally destroyed by the perturbation, and the EP no longer exists which will limit the enhancement for multiple sensing schemes in a time sequence. In this case, it is necessary to develop an EP condition nondemolition enhanced sensing mechanism to break the limit.

In this paper, we propose a novel EP-based enhanced sensing mechanism that relies on the shift of an EP in contrast to the conventional method of diverging from an EP. For the enhanced mechanism based on diverging from an EP, the perturbation breaks the EP condition, and it further deteriorates the EP enhance performance for implementing multiple sensing in a time sequence. Compared with diverging from an EP mechanism, the enhanced sensing mechanism based on shifting an EP demonstrates a slight shift along the parameter axis induced by the perturbation resulting in a remarkable enhancement for the frequency splitting. For the shift of an EP, there exists an EP in parameter space after perturbation, and one can prepare the system back to an EP state that promises the most effective enhancement for every sensing. Furthermore, we propose a mass sensor and a gyroscope scheme based on shifting an EP to verify the enhanced sensing mechanism. This work opens up paths to design ultrasensitive sensors and verifies potential applications in various fields including precision measurement and quantum metrology.

Results

Two enhanced sensing mechanisms based on an EP

Considering a 2-level coupled system composed of 2 modes represented by a_1 and a_2 as illustrated by the inset of Fig. 1A, the dynamical equations of the general coupled system can be written as

$$\frac{d}{dt}\begin{pmatrix} a_1 \\ a_2 \end{pmatrix} = -i\begin{pmatrix} \omega_1 - i\gamma_1 & J \\ J & \omega_2 - i\gamma_2 \end{pmatrix}\begin{pmatrix} a_1 \\ a_2 \end{pmatrix}, \quad (1)$$

where t can be the evolution time and the propagation distance. The resonance frequency and the decay of a_1 (a_2) are represented by ω_1 (ω_2) and γ_1 (γ_2), respectively. J denotes the coupling coefficient, and it can be real or complex. For the purpose of conciseness, we only consider the reciprocal coupling case and the similar conclusion can be obtained for the nonreciprocal coupling. Assuming that the solutions have the harmonic form $a_{1,2} = a_{1,2}e^{-i\lambda t}$, the eigenvalues of the coupled system can be expressed as

$$\lambda_{\pm} = \omega_{\text{mean}} - i\gamma_{\text{mean}} \pm \sqrt{(\omega_{\text{diff}} + i\gamma_{\text{diff}})^2 + J^2}. \quad (2)$$

$\omega_{\text{mean}} = (\omega_1 + \omega_2)/2$ and $\gamma_{\text{mean}} = (\gamma_1 + \gamma_2)/2$ represent the mean values of the resonance frequency and the loss. $\omega_{\text{diff}} = (\omega_1 - \omega_2)/2$ and $\gamma_{\text{diff}} = (\gamma_1 - \gamma_2)/2$ are the differences of the frequency and the decay. It can be indicated that when the parameter values meet the requirement $\pm iJ = \omega_{\text{diff}} + i\gamma_{\text{diff}}$, the system is prepared on an EP state.

The perturbation introduced to the sensor systems can induce frequency shift [3,31], linewidth broadening [45,46], or both. For the sake of simplicity, we consider the case that the perturbation only induces frequency shift to illustrate the difference between the 2 enhanced sensing mechanisms based on an EP.

If the coupling coefficient J is a real number and the enhanced sensing mechanism is well known as the eigenvalues diverging from an EP, the enhanced sensing mechanism based on the eigenvalues diverging from an EP after the perturbation ε is illustrated by Fig. 1B and C. The solid lines and the dashed lines represent the evolution of the 2 eigenvalues along with the system parameter J before and after introducing the perturbation. Usually, before introducing perturbation, the sensing system is prepared near an EP and one can monitor the frequency shift $\text{Re}[\Delta\lambda]$ and the linewidth change $\text{Im}[\Delta\lambda]$ after the perturbation. According to the frequency shift, the strength of the perturbation ε can be indicated. Due to the singularity of EPs, the frequency shifts of the eigenvalues obtain $\varepsilon^{1/2}$ (the red dashed line in Fig. 1D) enhancement comparing to the diabolic point (DP) (the blue solid line in Fig. 1D) in the condition of $\varepsilon \ll 1$. In contrast to EP, some microcavities support modes also with degenerate eigenvalues, but the associated eigenvectors can always be chosen to be orthogonal to each other, also known as DP. For the traditional cavity-based sensing schemes, the DP is utilized and the perturbation-induced frequency shift response is proportional to the perturbation strength, which is shown by the blue solid line in Fig. 1D. The inset of Fig. 1D indicates the frequency shift value is proportional to $\varepsilon^{1/2}$ as the slope is 1/2 in a logarithmic scale. To demonstrate the enhancement of EPs, the enhancement factor can be defined as

$$\eta = \left| \frac{Re[\Delta\lambda]}{\varepsilon} \right|. \quad (3)$$

Figure 1E illustrates the enhancement factor of an EP (the red dashed line) and a DP (the blue solid line) versus the perturbation strength. It can be indicated that an EP enhance performance is much better in the weak perturbation regime, which is consistent with the analysis above. It can be inferred that the EP condition is destroyed by the perturbation and the EP no longer exists in the parameter space for the enhanced sensing mechanism based on diverging from an EP. In the case of implementing multiple sensing in a time sequence, the enhancing performance deteriorates as the number of sensing

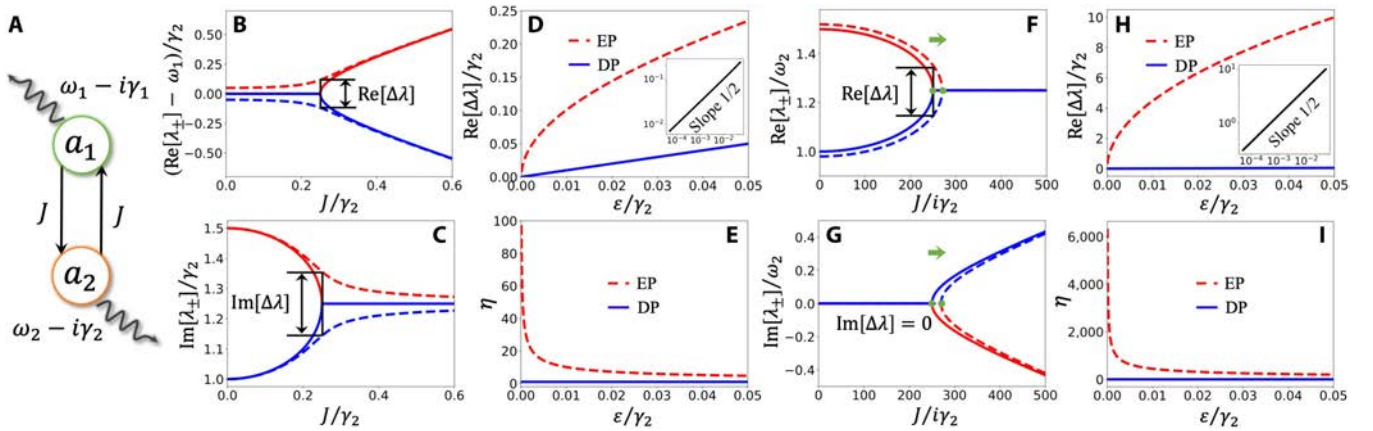


Fig. 1. The general model. (A) The schematic of the coupled 2-level system. The real parts (B) and the imaginary parts (C) of the eigenvalues versus J before (solid lines) and after (dashed lines) introducing the perturbation for the enhanced sensing mechanism based on diverging from an EP. $\omega_1/\gamma_2 = \omega_2/\gamma_2 = 1,500$, $\gamma_1/\gamma_2 = 1.5$, and $\varepsilon/\gamma_2 = 0.05$. (D) $\text{Re}[\Delta\lambda]$ versus the strength of the perturbation ε in the case of diverging from an EP (red dashed line) and a DP (blue solid line). The inset indicates $[\text{Re}\Delta\lambda]$ versus ε in the case of diverging from an EP in a logarithmic scale. (E) The enhancement factor of sensors based on diverging from an EP (red dashed line) and a DP (blue solid line). $\omega_1/\gamma_2 = \omega_2/\gamma_2 = 1,500$, $\gamma_1/\gamma_2 = 1.5$, and $J/\gamma_2 = 0.25$. The real parts (F) and the imaginary parts (G) of the eigenvalues versus J before (solid lines) and after (dashed lines) introducing the perturbation for the enhanced sensing mechanism based on shifting an EP. The green dots represent the location of EPs. $\omega_1/\gamma_2 = 1,500$, $\omega_2/\gamma_2 = 1,000$, $\gamma_1/\gamma_2 = 1$, and $\varepsilon/\gamma_2 = 20$. (H) $\text{Re}[\Delta\lambda]$ versus the strength of the perturbation ε in the case of shifting an EP (red dashed line) and a DP (blue solid line). The inset indicates $\text{Re}[\Delta\lambda]$ versus ε in the case of shifting an EP in a logarithmic scale. (I) The enhancement factor of sensors based on shifting an EP (red dashed line) and a DP (blue solid line). $\omega_1/\gamma_2 = 1,500$, $\omega_2/\gamma_2 = 1,000$, $\gamma_1/\gamma_2 = 1$, and $J/i\gamma_2 = 250$.

Table. The enhanced sensing mechanisms for different perturbations and coupling systems.

Perturbation induces	Real coupling systems	Imaginary coupling systems
Frequency shift	Diverging from an EP	Shift of an EP
Linewidth broadening	Shift of an EP	Diverging from an EP

increases as every next detection is conducted on the basis of being destroyed by the previous detection.

The shift of an EP mechanism requires the coupling coefficient is an imaginary number and can also exhibit $\varepsilon^{1/2}$ enhancement. The imaginary coupling between the 2 modes have been experimentally realized in dissipative coupled systems including atomic systems [47,48], optical systems [3,49,50], mechanical systems [9], circuits [51], and thermal materials [52]. Under some specific parameter values, the existence of the EP can be maintained along with a shift in the parameter space after the perturbation which is denoted by Fig. 1F and G. Due to the topological structure near an EP, the shift of an EP will lead to similar enhancement results to the sensing performance based on the eigenvalues diverge. The response of eigenvalues to the strength of perturbation and the enhancement factor of shifting an EP mechanism are demonstrated in Fig. 1H and I, respectively. On the other hand, the linewidth changes of the 2 eigenstates demonstrate different behaviors. In the case of an EP shift sensing, the 2 linewidths of the eigenstates stay the same as before the perturbation, which may further improve the enhancement performance in the perspective of experiments. The unbroadened linewidths after the perturbation may improve the precision of dispersion measurement. Another interesting point is there also exists an EP in the parameter space after the perturbation for the sensors based on shifting an EP which is an EP condition nondemolition enhanced sensing mechanism. One can prepare the system back to an EP state by tuning corresponding parameters after introducing the perturbation. In the case of the influence of the perturbation to the sensor that is hard to eliminate such as mass sensor and nanoparticle sensing, it is a challenging task to separate the deposited mass or nanoparticle and the sensing system, and the sensors based on shifting an EP will always obtain the most efficient enhancement as the system can be prepared back to an EP before the next sensing. Thus, for the task of implementing multiple sensing in a time sequence, sensors based on shifting an EP will always demonstrate the most effective EP enhancement for every detection.

As a conclusion, we demonstrate that the 2 enhanced sensing mechanisms based on an EP for the perturbation only induces frequency shift, and the case that the linewidth broadening induced by the perturbation is similar to the case we consider here. The conclusions for the 2 different systems can be found in Table.

Mass sensor based on shifting an EP

Optomechanics [53] has been a promising platform to investigate fundamental phenomena [54–58] and applied science [59–64]. Benefiting from abundant manipulation methods, realization of ultrasensitive sensors operating at EPs in optomechanical systems has gained wide attention over the last few decades. To illustrate the enhanced mechanism based on shifting an EP, here, we propose an optomechanical mass sensor. The mass sensor system as illustrated by Fig. 2A consists of 2 mechanical vibrators b_1 and b_2 coupling to the same optical field a with frequency ω_a and loss κ_a. The Hamiltonian of the system is ($\hbar = 1$)

$$H_m = \Sigma_{j=1,2}\left[\omega_{mj} b_j^\dagger b_j + g_j a^\dagger a\left(b_j + b_j^\dagger\right)\right] + \omega_a a^\dagger a + i\sqrt{\kappa_{ex}}\epsilon\left(a^\dagger e^{-i\omega_d t} - a e^{i\omega_d t}\right) \quad (4)$$

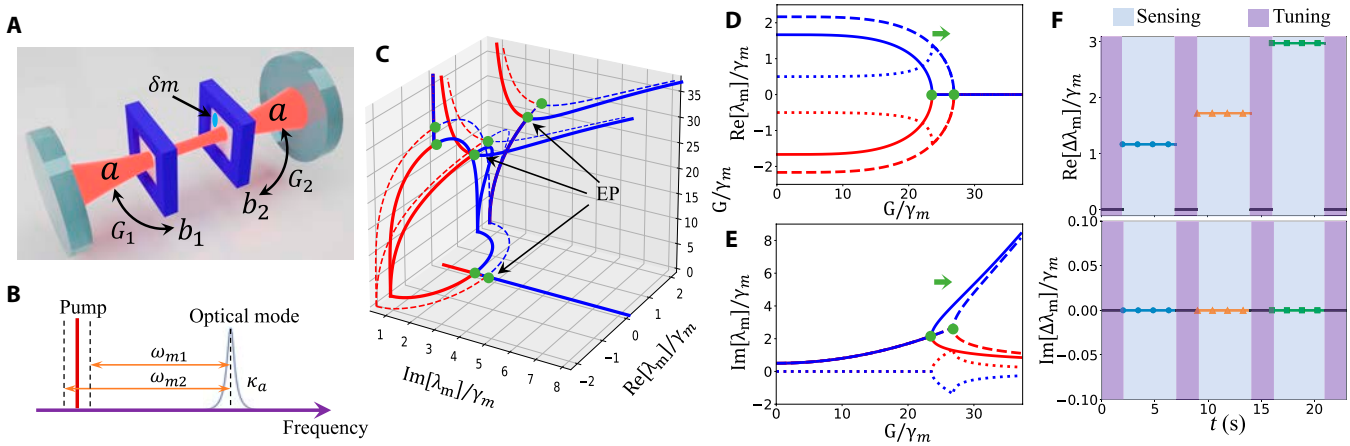


Fig. 2. Mass sensor based on shifting an EP. (A) The mass sensor schematic. (B) The pump scheme in frequency domain. (C) The evolution of the eigenvalues under different optomechanical coupling strength G. EPs are denoted by the green dots. (D and E) The real parts and the imaginary parts of the mass sensor system versus G. The solid lines and the dashed lines represent before and after introducing a deposited mass, respectively. The dotted lines are the differences between the eigenvalues before and after the perturbation. $\delta\omega = 0.0005\omega_1$. (F) The differences of the real parts and the imaginary parts for implementing multiple mass sensing in a time sequence. The corresponding frequency shifts are $\delta\omega = 0.0001\omega_1$, $0.0002\omega_1$, and $0.0005\omega_1$, respectively. The other parameters are $\omega_{m1}/2\pi = 6$ GHz, $\omega_{m2}/2\pi = 6.01$ GHz, $\gamma_{m1}/2\pi = \gamma_{m2}/2\pi = \gamma_m/2\pi = 3$ MHz, and $\kappa_a/2\pi = 2$ GHz.

The mechanical resonator b_j is characterized by the frequency ω_{mj} and the damping rate γ_{mj} $(j = 1, 2)$. g_j is the single-photon optomechanical coupling strength between the mechanical mode b_j and the optical mode a. κ_{ex} represents the coupling loss. Figure 2B represents the driving scheme of the mass sensor in frequency domain. The pump laser owns the driving frequency ω_d and the amplitude ϵ. Following the standard optomechanical linearization procedure and adiabatically eliminate the optical field, one can obtain the effective Hamiltonian of the system in the matrix form

$$H_m^{\text{eff}} = \begin{pmatrix} \Omega_0 - i\left(\frac{\gamma_{m1}}{2} + \frac{2G_1^2}{\kappa_a}\right) & -i\frac{2G_1G_2}{\kappa_a} \\ -i\frac{2G_1G_2}{\kappa_a} & -\Omega_0 - i\left(\frac{\gamma_{m2}}{2} + \frac{2G_2^2}{\kappa_a}\right) \end{pmatrix}, \quad (5)$$

where $\Omega_0 = (\omega_{m1} - \omega_{m2})/2$. $G_i = g_i\sqrt{n}$ is the effective optomechanical coupling strength with n denoting the intracavity photon number. $\kappa_a = \kappa_{ex} + \kappa_0$ represents the total loss rate of the optical mode. κ_0 indicates the intrinsic loss of the cavity mode. For convenience, we can set $G_1 = G_1 = G$ and $\gamma_{m1} = \gamma_{m2} = \gamma_m$. The eigenvalues of H_m^{eff} are given by

$$\lambda_{m\pm} = -i\left(\gamma_m/2 + \Gamma\right) \pm \sqrt{\Omega_0^2 - \Gamma^2}, \quad (6)$$

where $\Gamma = 2G^2/\kappa_a$. Note that the Hamiltonian form in Eq. 5 satisfies anti-parity time (PT) symmetry with an EP at $\Gamma = |\Omega_0|$. The evolution of the eigenvalues under different optomechanical coupling strengths are illustrated by the solid lines in Fig. 2C to E. Note that the locations of EPs are marked by the green dots in Fig. 2C.

For a traditional mass sensor, the relationship between the deposited mass δm and the caused frequency shift $\delta\omega$ can be given by [65]

$$\delta\omega = \frac{\omega_{m2}}{2m}\delta m = R\delta m. \quad (7)$$

$R = \omega_{m2}/2m$ represents the mass responsivity. ω_2 and m are the resonant frequency and the effective mass of the mechanical resonator supporting the deposition.

After depositing mass δm into the mechanical resonator b_2, the effective Hamiltonian of the system is

$$H_m^{\text{eff}'} = \begin{pmatrix} \Omega_0' - i\left(\frac{\gamma_{m1}}{2} + \frac{2G_1^2}{\kappa_a}\right) & -i\frac{2G_1G_2}{\kappa_a} \\ -i\frac{2G_1G_2}{\kappa_a} & -\Omega_0' - i\left(\frac{\gamma_{m2}}{2} + \frac{2G_2^2}{\kappa_a}\right) \end{pmatrix}, \quad (8)$$

where $\Omega_0' = \left(\omega_{m1} - \omega_{m2} - \delta\omega\right)/2$. After introducing the mass, the EP will move from the former point in the parameter space as Fig. 2C to E shown. The dashed lines demonstrate the evolution of the eigenvalues after the perturbation. In Fig. 2D and E, the dotted lines show the difference between the eigenvalues before and after, i.e., $\text{Re}[\lambda_m]_{\text{after}} - \text{Re}[\lambda_m]_{\text{before}}$ and $\text{Im}[\lambda_m]_{\text{after}} - \text{Im}[\lambda_m]_{\text{before}}$. It can be noticed that the deposited mass causes the shift of the EP and further lead to the largest frequency shift near the EP. Meanwhile, the introduction of the deposited mass will not change the bandwidth of the eigenstate, which theoretically boosts the sensitivity enhancement for EP-based sensors.

One can implement multiple mass sensing in a time sequence utilizing the mass sensor based on shifting an EP as it can be tuned back to an EP after each sensing period. Figure 2F demonstrates the differences of the real parts and the imaginary parts. There are 2 periods, sensing period and tuning period, during the time sequence mass sensing. During the sensing periods, the frequency shifts obtain the most effective enhancement and present mass-dependent response. The corresponding frequency shifts due to the deposited mass are $\delta\omega = 0.0001\omega_1$, $0.0002\omega_1$, and $0.0005\omega_1$, respectively. During the tuning periods, the system can be prepared back to an EP by tuning the optomechanical coupling strength. Note that no matter the system experiences sensing periods or tuning periods, the linewidths of the sensor are always the same as the unperturbed system as shown in Fig. 2F.

Gyroscope based on shifting an EP

The gyroscope scheme based on shifting an EP is illustrated by Fig. 3A. Two whispering-gallery-mode (WGM) cavities are coupled to 2 drop-filter waveguides with center-to-center distance L. On the basis of the 2 resonator modes $\Psi = (a_1, a_2)^{\top}$, the effective Hamiltonian in matrix form can be expressed as [66]

$$H_g^{\text{eff}} = \begin{pmatrix} \omega_{a1} - i\frac{\gamma_{\text{eff1}}}{2} & -ie^{i\varphi}\sqrt{\kappa_1\kappa_2} \\ -ie^{i\varphi}\sqrt{\kappa_1\kappa_2} & \omega_{a2} - i\frac{\gamma_{\text{eff2}}}{2} \end{pmatrix}, \quad (9)$$

where ω_{a1} and ω_{a2} are the resonance frequencies of the 2 WGM resonators. $\gamma_{\text{eff}j} = \Gamma_j + 2\kappa_j$ denotes the effective loss and Γ_j represents the intrinsic loss rate in the jth resonator. κ_j is the coupling rate between the jth resonator and the drop-filter waveguide. The phase delay factor is $\varphi = 2\pi n_w L/\lambda$, with n_w being the refractive index of waveguides and λ representing the wavelength of the light.

Benefiting from the tunability of the phase delay, the indirectly coupling system can exhibit anti-PT symmetry [9,47,52,67]. Without losing of generality, we can assume the 2 resonators have the equal losses $\Gamma_1 = \Gamma_2$ and the waveguide-resonator coupling rates are equal $\kappa_1 = \kappa_2 = \kappa$. Thereby, the effective Hamiltonian in anti-PT symmetry form is

$$H_g^{\text{eff}'} = \begin{pmatrix} \Omega_- - i\left(\frac{\Gamma_1+\Gamma_2}{4} + \kappa\right) & i\kappa \\ i\kappa & -\Omega_- - i\left(\frac{\Gamma_1+\Gamma_2}{4} + \kappa\right) \end{pmatrix}. \quad (10)$$

Here, $\Omega_- = (\omega_{a1} - \omega_{a2})/2$. When introducing rotation frequency into the first WGM resonator, the resonance frequency experiences a Sagnac frequency shift associated with the rotation direction

$$\Delta_{\text{Sag}} = \frac{nR\Omega\omega_{a1}}{c}\left(1 - \frac{1}{n^2} - \frac{\lambda}{n}\frac{\mathrm{d}n}{\mathrm{d}\lambda}\right), \quad (11)$$

where n and R are the refractive index and the radius of the resonator, respectively. c denotes the speed of the light, and the dispersion term $\mathrm{d}n/\mathrm{d}\lambda$ is relatively small in typical materials (~1%) [68]. For convenience, we define the sign of the rotation frequency depending on the rotation direction. As shown in Fig. 3A and B, in the case of counterclockwise (CCW) rotation

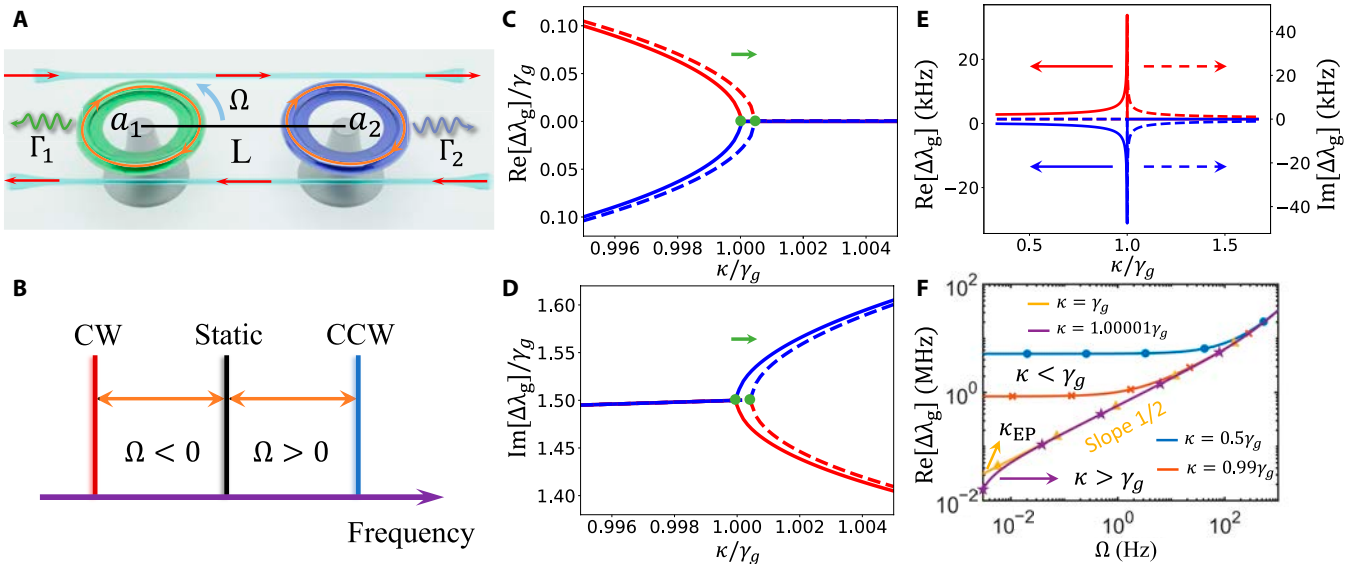


Fig. 3. Gyroscope based on shifting an EP. (A) The gyroscope schematic. (B) The Sagnac frequency shift due to the introduction of rotation. The black line represents the static resonant frequency of the optical mode a_1. The red (blue) frequency shift is corresponding to the CW (CCW) rotation direction, which is denoted by the red (blue) line. (C) The real parts and (D) the imaginary parts of the eigenvalues of the system as a function of κ/γ_g. The solid (dashed) lines are corresponding to the case without (with) a rotation. $\Omega = 0.1$ Hz. (E) The differences of the real parts and the imaginary parts of the eigenvalues before and after rotation under different values of κ. $\Omega = 0.1$ Hz. (F) Dependence of frequency splitting on the rotation frequency Ω in the case of anti-PT broken phase ($\kappa < \gamma_g$), anti-PT symmetry phase ($\kappa > \gamma_g$), and at an EP (κ_{EP}). The other parameters are $n = 1.44$, $R = 9$ mm, $c = 3 \times 10^8$ m/s, $\lambda = 1,550$ nm, and $\Omega_- = \Gamma_1 = \Gamma_2 = \gamma_g = 3$ MHz.

the sign of the rotation frequency is defined as positive associating with a positive Sagnac frequency shift and vice versa. For the case gyroscope experience clockwise (CW) rotation, the resonant frequency of a_1 has a red shift as indicated in Fig. 3B. Due to the definition of the sign of the rotation frequency, one can simply add the perturbation matrix into Eq. 10 after introducing rotation

$$H_g^{\text{eff}''} = \begin{pmatrix} \Omega_- + \Delta_{\text{Sag}} - i\left(\frac{\Gamma_1+\Gamma_2}{4}+\kappa\right) & i\kappa \\ i\kappa & -\Omega_- - i\left(\frac{\Gamma_1+\Gamma_2}{4}+\kappa\right) \end{pmatrix} \tag{12}$$

And the eigenvalues of the effective Hamiltonian are

$$\lambda_{g\pm} = \frac{\Delta_{\text{Sag}}}{2} - i\left(\frac{\Gamma_1+\Gamma_2}{4}+\kappa\right) \pm \sqrt{\left(\frac{\Delta_{\text{Sag}}+2\Omega_-}{2}\right)^2 - \kappa^2}. \tag{13}$$

It is clear that no matter the system experiences rotation or not, there is always a threshold coupling strength at $(\Delta_{\text{Sag}} + 2\Omega_-)/2$. The real parts and the imaginary parts of $\lambda_{g\pm}$ are illustrated by Fig. 3C and D. In the absence of the rotation, there are 3 regimes for different values of κ and the threshold is $\kappa_{\text{EP}} = \Omega_- = \gamma_g$. In the domain of $\kappa < \gamma_g$, the eigenstates share the same linewidth while possessing different resonance frequency and the system is in the anti-PT broken phase. In the case of $\kappa > \gamma_g$, the 2 eigenvalues have equal real part and different imaginary parts, which indicates that the system is in the anti-PT symmetry phase. The EP is the phase transition point of anti-PT symmetry phase and anti-PT broken phase. It is indicated that the EP is shifting along the parameter axis κ/γ_g after introducing a rotation. With the presence of the rotation, one can tune the system back to an EP state by adjusting the distance between the waveguides and the WGM cavities. Figure 3E shows the differences of the real parts and the imaginary parts of the eigenvalues before and after rotation, i.e., $\text{Re}[\lambda_g]_{\text{after}} - \text{Re}[\lambda_g]_{\text{before}}$ and $\text{Im}[\lambda_g]_{\text{after}} - \text{Im}[\lambda_g]_{\text{before}}$. The solid lines and the dashed lines denote the real parts and the imaginary parts, respectively. One can see near an EP that the system demonstrates a great frequency splitting and meanwhile maintains the linewidth.

After introducing rotation into the system, the reactions of the frequency splitting $\text{Re}[\Delta\lambda] = |\text{Re}[\lambda_{g+}] - \text{Re}[\lambda_{g-}]|$ in 3 regimes are not the same. Figure 3F illustrates the logarithmic behavior of the frequency splitting under different rotations in the case of anti-PT symmetry phase ($\kappa > \gamma_g$), anti-PT broken phase ($\kappa < \gamma_g$), and at the EP (κ_{EP}). In the case of the anti-PT broken phase, the frequency splitting is largest while the slope is smallest for the same perturbation strengths. However, for a small rotation frequency, the slope of the response at an EP is 1/2, which is predicted by the perturbation theory [4]. For a relatively large rotation frequency, the perturbation theory no longer works, and therefore, the slope of the response is larger than 1/2.

Conclusion

We propose a novel enhanced sensing mechanism based on perturbation-induced shift of an EP in contrast to the widely investigated method of diverging from an EP. Diverging from an EP mechanism destroys the EP condition in the parameter space and obtains $\varepsilon^{1/2}$ enhancement in the weak perturbation regime. In this case, the EP condition is totally destroyed by the perturbation and the EP no longer exists, which will limit the enhancement for multiple sensing schemes in a time sequence. To overcome the challenge, we propose the EP condition nondemolition enhanced sensing mechanism based

on shifting an EP, which demonstrates a slight shift along the parameter axis induced by the perturbation and also exhibits remarkable enhancement. The linewidths will maintain after the perturbation for the EP shift mechanism, which may improve the precision of dispersion measurement. To implement the EP shift sensing mechanism, we construct a mass sensor and a gyroscope sensing scheme for the mechanical modes and the optical mode pair, respectively. Combining other enhancing methods such as exceptional surfaces [30,69,70] and nonlinearity [38,71,72], the performance of sensors will be further improved. The enhanced sensing mechanism proposed in this paper provides a comprehensive understanding of EPs enhancing and may inspire technological development in various schemes.

Methods

In our numerical calculation, the frequencies and the linewidths of the modes are corresponding to the real parts and the imaginary parts of the eigenvalues of the system. These are crucial to the demonstration of EP and the influence of perturbation. For different types of perturbation, one can calculate the frequency and the linewidth of the system before and after introducing perturbation. The perturbation strength can be inferred by monitoring the corresponding changes.

Acknowledgments

Funding: This work is supported by the National Natural Science Foundation of China (62131002), The Key Research and Development Program of Guangdong Province (2018B-030325002), Beijing Advanced Innovation Center for Future Chip (ICFC), and Tsinghua University Initiative Scientific Research Program.

Author Contributions: X.M. and G.-Q.Q. conceptualized the study. H.Z. discussed the details of the study. B.-Y.W. and D.L. provided useful suggestions to the presentation of the work. G.-Q.L. and G.-L.L. supervised the study. All authors were involved in the discussions and preparation of the manuscript.

Competing Interests: The authors declare that they have no competing interests.

Data Availability

All data relevant to this work are available in the manuscript and supporting information. The data are available from the corresponding author upon reasonable request.

References

1. Miri MA, Alù A. Exceptional points in optics and photonics. *Science*. 2019;363(6422):eaar7709.
2. Wang C, Sweeney WR, Stone AD, Yang L. Coherent perfect absorption at an exceptional point. *Science*. 2021;373(6260):1261–1265.
3. Lai YH, Lu YK, Suh MG, Yuan Z, Vahala K. Observation of the exceptional-point enhanced Sagnac effect. *Nature*. 2019;576(7785):65–69.
4. Chen W, Kaya Ozdemir S, Zhao G, Wiersig J, Yang L. Exceptional points enhance sensing in an optical microcavity. *Nature*. 2017;548:192–196.
5. Ozdemir SK, Rotter S, Nori F, Yang L. Parity–time symmetry and exceptional points in photonics. *Nat Mater*. 2019;18(8):783–798.
6. Peng B, Özdemir ŞK, Lei F, Monifi F, Gianfreda M, Long GL, Fan S, Nori F, Bender CM, Yang L. Parity–time-symmetric whispering-gallery microcavities. *Nat Phys*. 2014;10(37):394–398.
7. Berry MV. Physics of nonhermitian degeneracies. *Czechoslov J Phys*. 2004;54(10):1039–1047.
8. Xu H, Mason D, Jiang L, Harris J. Topological energy transfer in an optomechanical system with exceptional points. *Nature*. 2016;537(7618):80–83.
9. Zhang Q, Yang C, Sheng J, Wu H. Dissipative coupling-induced phonon lasing. *Proc Natl Acad Sci*. 2022;119(52):Article e2207543119.
10. Lu XY, Jing H, Ma JY, Wu Y. P T-symmetry-breaking chaos in optomechanics. *Phys Rev Lett*. 2015;114(25):Article 253601.
11. Choi Y, Kang S, Lim S, Kim W, Kim JR, Lee JH, An K. Quasieigenstate coalescence in an atom-cavity quantum composite. *Phys Rev Lett*. 2010;104(15):Article 153601.
12. Park JH, Ndao A, Cai W, Hsu L, Kodigala A, Lepetit T, Lo YH, Kanté B. Symmetry-breaking-induced plasmonic exceptional points and nanoscale sensing. *Nat Phys*. 2020;16:462–468.
13. Moritake Y, Notomi M. Switchable unidirectional radiation from Huygens dipole formed at an exceptional point in non-Hermitian plasmonic systems. *ACS Photonics*. 2023;10(3):667–672.
14. Li Y, Argyropoulos C. Exceptional points and spectral singularities in active epsilon-near zero plasmonic waveguides. *Phys Rev B*. 2019;99:Article 075413.
15. Bergholtz EJ, Budich JC, Kunst FK. Exceptional topology of non-Hermitian systems. *Rev Mod Phys*. 2021;93(1):Article 015005.
16. Qin GQ, Mao X, Zhang H, Wen PY, Li GQ, Ruan D, Long GL. Optomechanical compensatory cooling mechanism with exceptional points. *Phys Rev A*. 2022;106(6):Article 063510.
17. El-Ganainy R, Makris KG, Khajavikhan M, Musslimani ZH, Rotter S, Christodoulides DN. Non-Hermitian physics and PT symmetry. *Nat Phys*. 2018;14:11–19.
18. Liu S, Shao R, Ma S, Zhang L, You O, Wu H, Xiang YJ, Cui TJ, Zhang S. Non-Hermitian skin effect in a non-Hermitian electrical circuit. *Research*. 2021;2021:5608038.
19. Zhang J, Peng B, Özdemir ŞK, Pichler K, Krimer DO, Zhao G, Nori F, Liu YX, Rotter S, Yang L. A phonon laser operating at an exceptional point. *Nat Photonics*. 2018;12(8):479–484.
20. Lu H, Ozdemir S, Kuang LM, Nori F, Jing H. Exceptional points in random-defect phonon lasers. *Phys Rev Appl*. 2017;8(4):Article 044020.
21. Wang B, Liu ZX, Jia X, Xiong H, Wu Y. Polarization-based control of phonon laser action in a parity time-symmetric optomechanical system. *Commun Phys*. 2018;1:43.
22. Song Q, Odeh M, Zuniga-Perez J, Kante B, Genevet P. Plasmonic topological metasurface by encircling an exceptional point. *Science*. 2021;373(6559):1133–1137.
23. Zhang XL, Jiang T, Chan CT. Dynamically encircling an exceptional point in anti-parity time symmetric systems: Asymmetric mode switching for symmetry-broken modes. *Light: Sci Appli*. 2019;8:88.
24. Liu Q, Li S, Wang B, Ke S, Qin C, Wang K, Liu W, Gao D, Berini P, Lu P. Efficient mode transfer on a compact silicon chip by encircling moving exceptional points. *Phys Rev Lett*. 2020;124(15):Article 153903.

25. Hassan AU, Zhen B, Soljačić M, Khajavikhan M, Christodoulides DN. Dynamically encircling exceptional points: Exact evolution and polarization state conversion. *Phys Rev Lett*. 2017;118(9):Article 093002.
26. Long D, Mao X, Qin GQ, Zhang H, Wang M, Li GQ, Long GL. Dynamical encircling of the exceptional point in a largely detuned multimode optomechanical system. *Phys Rev A*. 2022;106(5):Article 053515.
27. Hodaei H, Hassan AU, Wittek S, Garcia-Gracia H, el-Ganainy R, Christodoulides DN, Khajavikhan M. Enhanced sensitivity at higher-order exceptional points. *Nature*. 2017;548(7666):187.
28. Xiao Z, Li H, Kottos T, Alù A. Enhanced sensing and nondegraded thermal noise performance based on p t-symmetric electronic circuits with a sixth-order exceptional point. *Phys Rev Lett*. 2019;123(21):Article 213901.
29. Wiersig J. Enhancing the sensitivity of frequency and energy splitting detection by using exceptional points: Application to microcavity sensors for single-particle detection. *Phys Rev Lett*. 2014;112(20):Article 203901.
30. Qin G-Q, Xie RR, Zhang H, Hu YQ, Wang M, Li GQ, Xu H, Lei F, Ruan D, Long GL. Experimental realization of sensitivity enhancement and suppression with exceptional surfaces. *Laser Photonics Rev*. 2021;15(5):2000569.
31. Djorwe P, Pennec Y, Djafari-Rouhani B. Exceptional point enhances sensitivity of optomechanical mass sensors. *Phys Rev Appl*. 2019;12(2):Article 024002.
32. Qin G-Q, Wang M, Wen J-W, Ruan D, Long G-L. Brillouin cavity optomechanics sensing with enhanced dynamical backaction. *Photonics Res*. 2019;7(12):1440.
33. Ren J, Hodaei H, Harari G, Hassan AU, Chow W, Soltani M, Christodoulides D, Khajavikhan M. Ultrasensitive micro-scale parity-time-symmetric ring laser gyroscope. *Opt Lett*. 2017;42(8):1556.
34. Kononchuk R, Kottos T. Orientation-sensed optomechanical accelerometers based on exceptional points. *Phys Rev Res*. 2020;2(2):Article 023252.
35. Mao X, Qin GQ, Yang H, Zhang H, Wang M, Long GL. Enhanced sensitivity of optical gyroscope in a mechanical parity-time-symmetric system based on exceptional point. *New J Phys*. 2020;22(9):Article 093009.
36. Li Z, Li C, Xiong Z, Xu G, Wang YR, Tian X, Yang X, Liu Z, Zeng Q, Lin R, et al. Stochastic exceptional points for noise-assisted sensing. *Phys Rev Lett*. 2023;130(22): Article 227201.
37. Nikzamir A, Rouhi K, Figotin A, Capolino F. Demonstration of exceptional points of degeneracy in gyrator-based circuit for high-sensitivity applications. arXiv. 2021.
38. Bai K, Fang L, Liu TR, Li JZ, Wan D, Xiao M. Nonlinearity-enabled higher-order exceptional singularities with ultra-enhanced signal-to-noise ratio. *Natl Sci Rev*. 2023;10(7): nwac259.https://doi.org/10.48550/arXiv.2107.00639
39. Kononchuk R, Cai J, Ellis F, Thevamaran R, Kottos T. Exceptional-point-based accelerometers with enhanced signal-to-noise ratio. *Nature*. 2022;607(7920):697.
40. Sahoo A, Sarma AK. Two-way enhancement of sensitivity by tailoring higher-order exceptional points. *Phys Rev A*. 2022;106(2):Article 023508.
41. Tu C, Yang MH, Zhang ZQ, Lv XM, Li L, Zhang XS. Highly sensitive temperature sensor based on coupled-beam aln-on-si mems resonators operating in out-of-plane flexural vibration modes. *Research*. 2022;2022:9865926.
42. Hokmabadi MP, Schumer A, Christodoulides DN, Khajavikhan M. Non-hermitian ring laser gyroscopes with enhanced sagnac sensitivity. *Nature*. 2019;576:70.
43. Wang H, Lai Y-H, Yuan Z, Suh M-G, Vahala K. Petermann-factor sensitivity limit near an exceptional point in a brillouin ring laser gyroscope. *Nat Commun*. 2020;11(1):1610.
44. Mao X, Yang H, Long D, Wang M, Wen PY, Hu YQ, Wang BY, Li GQ, Gao JC, Long GL. Experimental demonstration of mode-matching and sagnac effect in a millimeter-scale wedged resonator gyroscope. *Photonics Res*. 2022;10:2115.
45. Shao L, Jiang XF, Yu XC, Li BB, Clements WR, Vollmer F, Wang W, Xiao YF, Gong Q. Detection of single nanoparticles and lentiviruses using microcavity resonance broadening. *Adv Mater*. 2013;25(39):5616.
46. Shen B-Q, Yu XC, Zhi Y, Wang L, Kim D, Gong Q, Xiao YF. Detection of single nanoparticles using the dissipative interaction in a high-q microcavity. *Phys Rev Appl*. 2016;5(2):Article 024011.
47. Peng P, Cao W, Shen C, Qu W, Wen J, Jiang L, Xiao Y. Anti-parity–time symmetry with flying atoms. *Nat Phys*. 2016;12(12):1139.
48. Jiang Y, Mei Y, Zuo Y, Zhai Y, Li J, Wen J, du S. Anti-parity-time symmetric optical four-wave mixing in cold atoms. *Phys Rev Lett*. 2019;123(19):Article 193604.
49. Li Q, Zhang CJ, Cheng ZD, Liu WZ, Wang JF, Yan FF, Lin ZH, Xiao Y, Sun K, Wang YT, et al. Experimental simulation of anti-parity-time symmetric lorentz dynamics. *Optica*. 2019;6:67.
50. Bergman A, Duggan R, Sharma K, Tur M, Zadok A, Alù A. Observation of anti-parity-time-symmetry, phase transitions and exceptional points in an optical fibre. *Nat Commun*. 2021;12(1):486.
51. Choi Y, Hahn C, Yoon JW, Song SH. Observation of an anti-pt-symmetric exceptional point and energy-difference conserving dynamics in electrical circuit resonators. *Nat Commun*. 2018;9(1):2182.
52. Li Y, Peng YG, Han L, Miri MA, Li W, Xiao M, Zhu XF, Zhao J, Alù A, Fan S, et al. Anti–parity-time symmetry in diffusive systems. *Science*. 2019;364(6436):170.
53. Aspelmeyer M, Kippenberg TJ, Marquardt F. Cavity optomechanics. *Rev Mod Phys*. 2014;86:1391.
54. Weis S, Rivière R, Deléglise S, Gavartin E, Arcizet O, Schliesser A, Kippenberg TJ. Optomechanically induced transparency. *Science*. 2010;330(6010):1520.
55. Kim J, Kuzyk MC, Han K, Wang H, Bahl G. Non-reciprocal brillouin scattering induced transparency. *Nat Phys*. 2015;11:275.
56. Kronwald A, Marquardt F. Optomechanically induced transparency in the nonlinear quantum regime. *Phys Rev Lett*. 2013;111(13):Article 133601.
57. Qin G-Q, Yang H, Mao X, Wen JW, Wang M, Ruan D, Long GL. Manipulation of optomechanically induced transparency and absorption by indirectly coupling to an auxiliary cavity mode. *Opt Express*. 2020;28(1):580.
58. Wang K, Gao Y-P, Jiao R, Wang C. Recent progress on optomagnetic coupling and optical manipulation based on cavity-optomagnonics. *Front Phys*. 2022;17(4):42201.
59. Del'Haye P, Schliesser A, Arcizet O, Wilken T, Holzwarth R, Kippenberg TJ. Optical frequency comb generation from a monolithic microresonator. *Nature*. 2007;450(7173):1214.
60. Wang Y-D, Clerk AA. Using interference for high fidelity quantum state transfer in optomechanics. *Phys Rev Lett*. 2012;108(15):Article 153603.

61. Tian L. Adiabatic state conversion and pulse transmission in optomechanical systems. *Phys Rev Lett*. 2012;108(15):Article 153604.
62. Ruesink F, Mathew JP, Miri M-A, Alù A, Verhagen E. Optical circulation in a multimode optomechanical resonator. *Nat Commun*. 2018;9(1):1798.
63. Shen Z, Zhang YL, Chen Y, Sun FW, Zou XB, Guo GC, Zou CL, Dong CH. Reconfigurable optomechanical circulator and directional amplifier. *Nat Commun*. 2018;9(1):1797.
64. Domeneguetti RR, Zhao Y, Ji X, Martinelli M, Lipson M, Gaeta AL, Nussenzveig P. Parametric sideband generation in cmos-compatible oscillators from visible to telecom wavelengths. *Optica*. 2021;8(3):316.
65. Li M, Tang HX, Roukes ML. Ultra-sensitive nems-based cantilevers for sensing, scanned probe and very high-frequency applications. *Nat Nanotechnol*. 2007;2(2):114.
66. Peng Z-H, Jia C-X, Zhang Y-Q, Yuan J-B, Kuang L-M. Level attraction and PT symmetry in indirectly coupled microresonators. *Phys Rev A*. 2020;102(4):Article 043527.
67. Wu N, Cui K, Xu Q, Feng X, Liu F, Zhang W, Huang Y. On-chip mechanical exceptional points based on an optomechanical zipper cavity. *Sci Adv*. 2023;9(3):eabp8892.
68. Maayani S, Dahan R, Kligerman Y, Moses E, Hassan AU, Jing H, Nori F, Christodoulides DN, Carmon T. Flying couplers above spinning resonators generate irreversible refraction. *Nature*. 2018;558(7711):569.
69. Zhong Q, Ren J, Khajavikhan M, Christodoulides DN, Özdemir ŞK, el-Ganainy R. Sensing with exceptional surfaces in order to combine sensitivity with robustness. *Phys Rev Lett*. 2019;122(15):Article 153902.
70. Zhang X, Ding K, Zhou X, Xu J, Jin D. Experimental observation of an exceptional surface in synthetic dimensions with magnon polaritons. *Phys Rev Lett*. 2019;123(23):Article 237202.
71. Zhang H, Huang R, Zhang SD, Li Y, Qiu CW, Nori F, Jing H. Breaking anti-pt symmetry by spinning a resonator. *Nano Lett*. 2020;20(10):7594.
72. Silver JM, del Bino L, Woodley MTM, Ghalanos GN, Svela AØ, Moroney N, Zhang S, Grattan KTV, del'Haye P. Nonlinear enhanced microresonator gyroscope. *Optica*. 2021;8(9):1219.